

OBSERVATIONAL STUDIES OF TURBULENT TRANSFER PROCESSES ACROSS THE URBAN CANOPY

José M. Gálvez, Petra Klein, Sean Arms and Brian Bridges
University of Oklahoma, Norman, Oklahoma

1. INTRODUCTION

The role of the urban canopy on the turbulent transfer of heat and momentum with the atmosphere is investigated. Relevant studies described in the literature (i) have mainly focused on measurements above the roughness sub-layer, (ii) have been carried out using a reduced number of instrumentation platforms, or (iii) took place over short periods of time: generally during intensive observational campaigns. Furthermore, some of the results from these studies are limited in space and time, and in some instances, even contradictory. With these factors in mind, an interest arose in: (i) achieving a comprehensive understanding about flow-urban canopy interactions and how they modulate turbulent transfer processes within the urban roughness sub-layer, and (ii) understanding what the integrated role of the canopy on turbulent transfer processes is, and how the integrated effect relates to its individual components. The goal is addressed via a 1-year long observational campaign carried out in a set of three urban street canyons using thirteen sonic anemometers (SA) and one small aperture scintillometer (SLS). Since all instrumentation platforms functioned together since late March 2010, the analysis here presented is constrained to the April 1-June 30 2010 time frame.

It is also of particular interest to evaluate and use scintillometers as means to study the integrated role of the urban canopy on turbulent transfer processes. Among the platforms designed for the measurement of turbulence, scintillometers have the advantage of being able to measure quantities that are integrated in time and space. This skill is particularly useful over heterogeneous environments such as urban areas, where spatial and temporal representativeness is not easy to attain using only point measurements. The combination of SLS and SA measurements was designed to provide a means to understand how the street canyons modulate turbulent transfer as a whole, and how their individual components contribute to the integrated role.

The present study is funded by the NSF Career Award ILREUM (Innovative Laboratory for the Research and Education in Urban Meteorology). The strategy designed to study the role of the urban canopy within the context of ILREUM includes two three-month-long sub-urban campaigns, the core 1-year long urban campaign, and a 3-week long additional urban campaign carried out in a different urban setup. Given the large span of the ILREUM studies, only a few results from the core urban campaign are presented in this manuscript.

2. BACKGROUND

2.1. Scintillometry basics

Scintillometers are instruments designed to measure intensity fluctuations in electromagnetic waves. In the atmospheric surface layer, these fluctuations are caused by turbulence. Each SLS consists of a transmitter and a receiver, which can be separated by path lengths that vary between tens of meters and ten kilometers. The path length is tightly related to the emitted wavelength, and to the apertures of transmitter and receiver. Large aperture scintillometers operate at radio wavelengths and over kilometer-long paths, whereas small aperture ones operate at optical wavelengths and over shorter paths. The scintillometer used during ILREUM is a small aperture model, the SCINTEC SLS-20, and operates at a wavelength of 670 nm. The optimal path length ranges between 50 and 200 m. Furthermore, this type of scintillometer is bichromatic. This means that the transmitter emits two radiation beams with orthogonal polarizations, so their intensity fluctuations can be identified independently by the receiver. Having two beams does not only allow for the calculation of intensity fluctuation variances but also for the calculation of covariances, which ultimately lead to the direct calculation of inner scales of turbulence l_0 .

Some turbulence properties can be inferred from scintillometer measurements. While propagating through air, electromagnetic waves are exposed to atmospheric turbulence, which leads to refractive index scattering. When beam scattering is integrated over a long distance, the intensity signal captured by the receiver fluctuates. These intensity fluctuations

* Corresponding author address: José. M. Gálvez. Univ. of Oklahoma, School of Meteorology, Norman, OK, 73072-7307; e-mail: jmgalvez@ou.edu

are known as scintillations. Given the existence of a relationship between turbulence and scintillations, the latter can be used for the estimation of turbulent fluxes via the use of wave propagation and Monin-Obukhov similarity (MOS) theory. A diagram that illustrates the process required to obtain fluxes from scintillations is presented in Figure 1.

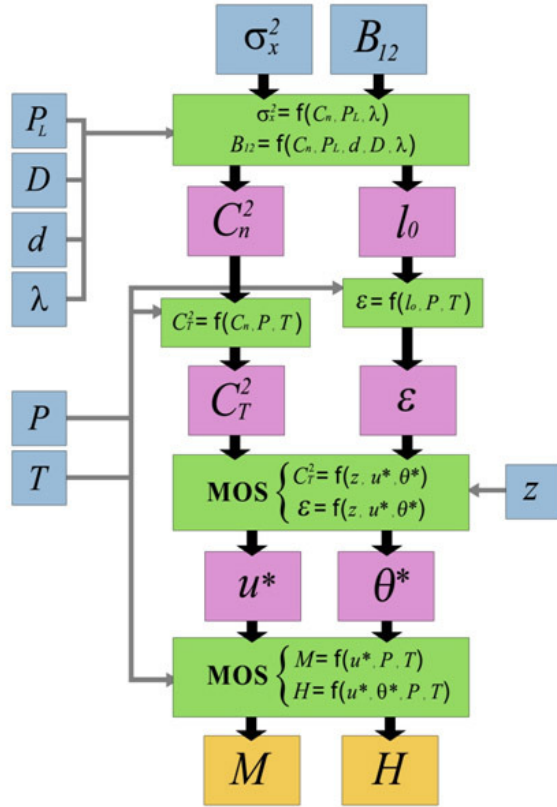


Figure 1. SCINTEC SLS-20 algorithm for the calculation of turbulent fluxes from scintillations.

Input variables and parameters in Figure 1 are indicated in blue; calculations in green; and output values in purple and peach. The variables measured by the SLS are σ_{12} and B_{12} , which are log-variances and log-covariances of intensity fluctuations. Inner scale of turbulence l_0 and structure function of refractive index fluctuations C_n^2 values can then be calculated with wave propagation theory expressions and the aid of four additional fixed parameters: path length P_L , transmitter aperture diameter D , receiver aperture diameter d and wavelength λ . It is also worth mentioning that a path-dependant weight function allows for most of the weight to be placed near the center of the path. This minimizes signal contamination by the instrument itself.

Dissipation rates of turbulent kinetic energy ϵ and the structure function of temperature fluctuations C_T^2 can then be calculated. The latter also requires the use of atmospheric temperature T and pressure P observations. In this case, it is assumed that values of C_n^2 can be explained only by the contribution of temperature fluctuations since studies have shown that moisture fluctuations C_q^2 become negligible over distances in the order of 50-200m. Once C_T^2 and ϵ are available, surface layer scales (u^* and θ^*) are calculated via iterations over MOS empirical expressions. Once u^* and θ^* are calculated, fluxes of heat H and momentum M can be obtained. The values of height above ground z (and displacement height d_0 , if needed) used in MOS become critical since they largely modulate the magnitude of fluxes.

2.2. Applicability in heterogeneous environments

An important question arises when scintillometers are operated over a non-homogeneous surface layer. Even more so in urban areas, where high complexity dominates and the basic assumptions for MOS are not fulfilled. It turns out that some authors have already shown that scintillometers can perform very well over complex environments once MOS expressions are modified. Kanda et al. (2002) evaluated scintillometer measurements locally for a few hours over an urban environment in Tokyo, Japan. They found modified versions of MOS equations that led to good agreement with EC heat fluxes measured at the same location. Although scintillometer measurements were a bit higher, the differences were lower than 10% for most values. Salmond et al. (2003) developed a modified version of MOS equations based upon environmental characteristics of the city of Basel, Switzerland. This was done as part of the Basel Urban Boundary Layer Experiment (BUBBLE) carried out during the summer of 2002. This work was later detailed in Roth et al. (2006). The methodology described used empirical fits via comparisons made using dissipation rate of turbulent kinetic energy, since they provide the only means of comparison that is independent of MOS.

3. METHODS

3.1. Urban measurement site

The core ILREUM urban campaign was carried out at a site located within the campus of the University of Oklahoma in the city of Norman, Oklahoma. The site lays about 4.5 km southeast of the site where the sub-urban campaigns were held. This was planned so that similar climatological flow and stability conditions could be used for comparison.

The geographical coordinates of the measurement site are 35°11'55" N, 97°26'34" W and 353 mASL.

The site consists of four long (~80 m) buildings separated by courtyards. Their distribution resembles morphologically -ideal street canyons. Building height is 11.8-m, width 13.8-m, and building separation varies between 50 m in the central street canyon and 30 m in the other two. The buildings are oriented east-west, which simplifies the analysis given that the prevailing wind direction (WD) in the area is from the south and allows for plenty of observations with across-canyon flow conditions. Surface types amongst canyons differ: the southernmost canyon is mostly paved with asphalt whereas the other two are covered mainly by grass, sparse trees and some sidewalks. A cross section of the site, looking west,

can be found in Figure 2. The sketch shows the four buildings, surface types that separate them and the instruments. Surface types include grass (green) and pavement (black). Instruments include thirteen SA and the SLS. Nine of the SA were manufactured by RMYoung, model 81000 and four by Campbell Scientific, model CSAT3. The SLS was manufactured by SCINTEC and the model is SLS-20. As figure 2 illustrates, five sonic anemometers (B1, B2, C1, C2, C3) are located over roof tops and the other eight (D1, D2, D3, E1, E2, E3, E4, F1) all concentrated on the central courtyard. The scintillometer is operated from the second building to the northernmost. No measurements were made over the southernmost courtyard, but some information about its thermal and turbulence properties can be inferred on the data collected by mast C1 when southerly flow is present.

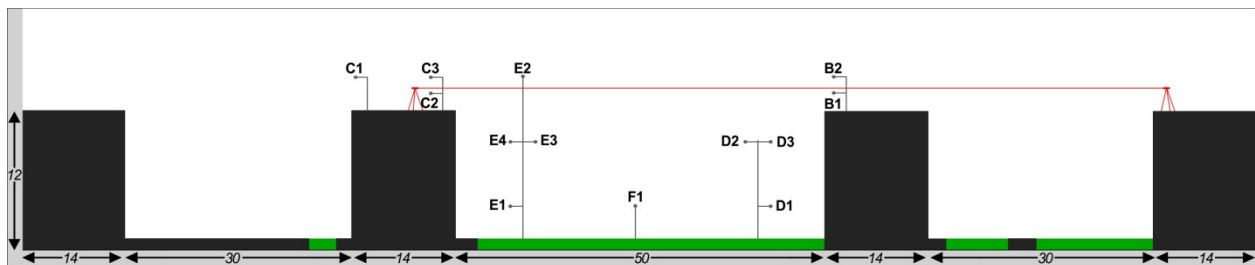


Figure 2. Cross section of the campaign site.

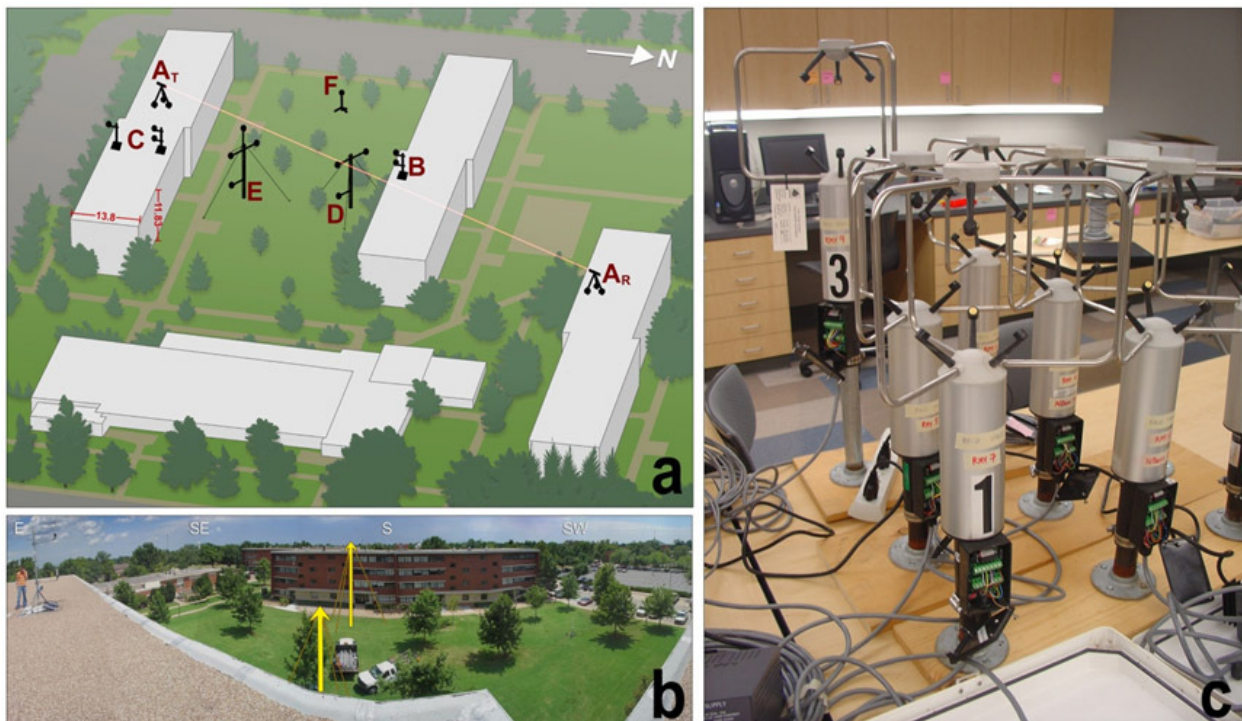


Figure 3. Birds-eye-view sketch of the campaign site (a). Panoramic photograph taken just west from Mast B (b). Since the courtyard towers had not been installed their future position is sketched in yellow. RMYoung sonic anemometers sitting at the laboratory prior to deployment (c).

Another view of the field campaign site is found in Figure 3. Panel (a) shows a representation of the site from a birds-eye-view perspective. It illustrates the presence of sidewalks, trees and provides with an idea of the obstacles around the site: a small building located to the east and a paved street that runs to the south and west. The latter plays a role when wind directions are from the south and west. Panel (b) shows a panoramic photograph of the measurement site. This picture was taken immediately west from mast B pointing south-southeastwards, and right before the courtyard towers (D and E) were installed. It captures roof mast B to the left, the potential location of towers D and E indicated with yellow arrows over the courtyard, and roof masts C, which are hard to distinguish behind the southernmost courtyard tower. Panel (c) shows some of the sonic anemometers being tested and set up at the laboratory before deployment.

3.2. Operation, data transmission and availability

The measurement site operated automatically. SA masts and the SLS transmitter were powered using solar panels and batteries, and the courtyard towers and SLS receiver by local energy sources. SA measurements were made continuously since June 2009 with a temporal resolution of 10Hz. Once data were collected, they were transmitted wirelessly to a computer and stored in a server automatically. SLS

data were collected continuously since March 2010 with a temporal resolution of 1-minute and also stored automatically. Short-lived interruptions on the data collection process were caused by rainfall, storms and rare power outages. Based on data completeness, the analysis period window selected ranged from April 1 and June 30 2010.

4. RESULTS: OVERVIEW

SA data are used to provide an overview of spatial and temporal distributions of meteorological fields in the urban site. The results here presented focus only on two contrasting flow regime scenarios: northerly (330° - 30° WD) and southerly (150° - 210° WD). Scenario selection was based upon 10-mAGL winds measured at the Norman MESONET site, considered as the reference from its location in a homogeneous environment. Scenario selection was also designed to study flow-canopy interactions in the context of turbulent transfer when across-canyon reference winds are present. The analysis is based on cross-sections and SA measurements only. General observations on scintillometer data and how they relate to SA observations will be addressed in section 5.

4.1. Flow characteristics

The general behavior of flow patterns measured during reference northerly and southerly flow regimes are summarized in Figures 4 and 5.

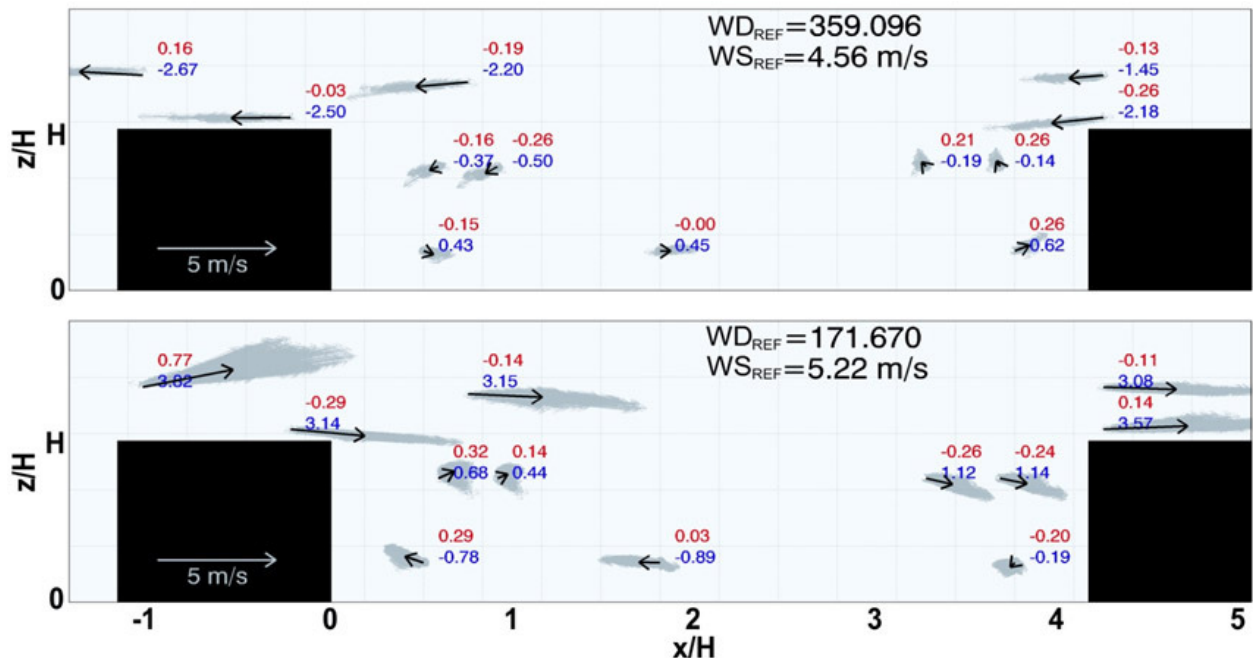


Figure 4. Cross-section of the mean flow vectors (black arrows) and scatter (gray arrows) measured during periods of reference northerly (top) and southerly (bottom) winds. Average u (blue) and w (red) values are also indicated. Mean reference WD in degrees and WS are also indicated.

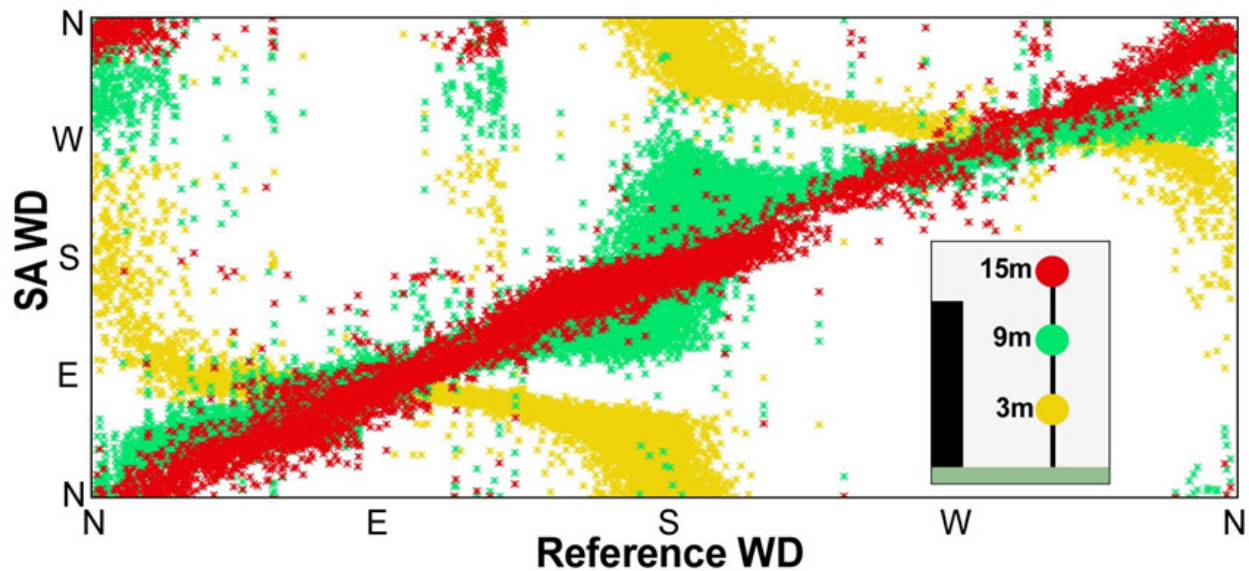


Figure 5. Wind directions measured with sonic anemometers at three levels (15-m in red; 9-m in green and 3-m in yellow) in the southern tower, plotted as a function of reference wind direction.

Figure 4 is a cross-section of the measurement site looking west. It shows mean (black arrows) and individual (gray arrows) wind vectors measured with SA during periods of northerly (top) and southerly (bottom) reference flow. Wind vectors are plotted using zonal and vertical components of velocity only. Figure 4 illustrates how the flow interacts with the canyon under across-canyon flow conditions. Some of the features evident are: (i) the presence of a shear layer that divides higher velocities above building height H with lower velocities inside the canyon; (ii) the generation of a rotor inside the canyon with sinking flow in the downwind side and a narrower region of rising motion in the lee side; (iii) the presence of sinking flow over the edge of the buildings in the upwind side of the canyon; (iv) the presence of a narrow region of rising flow over the downwind edge of the canyon; (v) the occurrence of sinking flow near and above the shear layer over most of the canyon width, which suggest prevailing flow penetration into the canyon from the top; (vi) the presence of strong rising flow ($\bar{w}=0.77 \text{ ms}^{-1}$) and large horizontal velocities near the southern edge of the southernmost building under southerly flow conditions. The cause seems to be flow channeling by the building located further south, and enhanced vertical motions from strong heating that results from the thermal properties of asphalt.

Figure 5 illustrates the behavior of WD at three heights inside the canyon, plotted as a function of reference WD. The purpose was to (i) describe the vertical structure of the flow inside the canyon where

SA at three different levels were available and (ii) explore whether these data could suggest regions of canyon flow exit, since Figure 4 suggested the presence of sinking flow into the canyon along most of the upper boundary.

The results illustrate how WD is modified as winds penetrate inside the canyon. The uppermost level (in red) is located just above the shear layer, and exhibits very similar WD when compared to reference values (linear trend). A slight deviation in the counterclockwise sense suggests effects of obstacles on a regional scale. Winds inside the canyon show the effects of channeling. As winds penetrate, the zonal component of WD increases and reaches a maximum somewhere between the 3 and 9-m level. At this point, winds are mainly from the east or west, which suggests the presence of flow exit regions at this level. Further inside the canyon, at 3-m, WD generally opposes to that of the reference flow since the SA is placed inside the return flow section of the rotor that develops inside the canyon.

4.2. Specific cases

Timeseries of relevant meteorological variables are shown in Figure 6. Sensible heat fluxes from the top measurement height (15-mAGL) are shown in the top panels; WD and WS information on the central panels; and air temperature (red), relative humidity (green) and solar radiation (yellow) in the bottom panels. Except for flux data, all additional information was provided by the Norman MESONET.

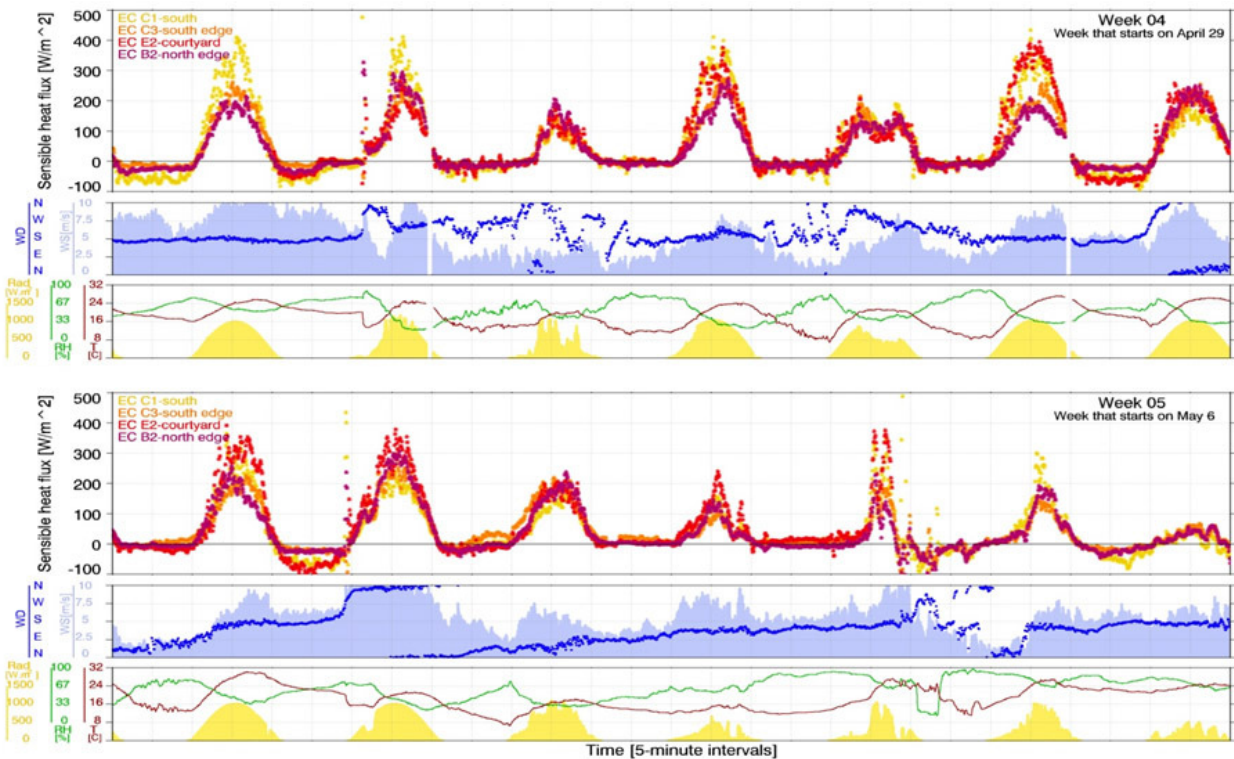


Figure 6. Raw timeseries of some meteorological variables measured between April 29 and May 13, 2010.

Diurnal and intra-diurnal variability of sensible heat fluxes can be observed in Figure 6. Diurnal cycles are clearly discernable, with near neutral or slightly negative sensible heat flux (SHFX) values during the night and larger positive values during the day. Nighttime fluxes can be as large as -100 Wm^{-2} , but they generally remain between 0 or slightly above and -20 Wm^{-2} . Nights with above-zero SHFX values suggest that the release of heat stored during the day may be playing a role, as it does in most urban environments. Daytime values of SHFX can be as high as $+400 \text{ Wm}^{-2}$, but they generally oscillate between 100 and 300 Wm^{-2} . The effect of different weather conditions seems to play an important role on intra-diurnal variability as discussed in the following.

As expected, the factor that seems to be the most important modulator of SHFX magnitude is solar radiation (yellow). Daytime SHFX largely decrease when clouds are present, and the shape of their diurnal cycles somewhat resembles the shape of the diurnal cycles of solar radiation. Another factor is WS, which is directly proportional to the magnitude of SHFX. This is particularly evident at nighttime, when intra-diurnal variations are larger: more negative SHFX develop under stronger WS. Examples are the last night of the first week (May 5, 2010) and the second night of the second week (May 7, 2010).

WD, as expected, seems to play a role as well. The reason is that different reference WD interact with different obstacles and lead to different fetches of origin of SHFX values. The determination of fetch is also a function of WS, but the combined effect of WD and WS will not be here addressed. Southerly WD lead to larger SHFX. Although not many periods with northerly flow were present during period described, SHFX during these exhibit smaller magnitudes. Other interesting features in the timeseries arise from the arrival of frontal systems. This is evident on the second day of each week, and leads to a sudden increase on the scatter of SHFX values.

SA location within the canopy also plays an important role on SHFX distribution and is evident from differences between SA under given weather conditions. Some of these differences persist under similar flow regimes, and suggest that WD and WS play an important role on SHFX modulation. For example, the largest daytime SHFX values occur at C1 (yellow) and E2 (red) during periods of southerly flow. During periods of northerly flow, however, the largest values occur at B2 (in purple). Large negative fluxes occur at C1 and B1 but not at B2, located closer to the roof.

4.3. SHFX and TKE cross sections

SHFX and TKE across the central courtyard are studied via cross-sections (CS) displayed in Figures 7, 8 and 9. Plotted fields include wind vectors (v, w), SHFX (large numbers and shading) and TKE (small numbers) stratified for northerly (top) and southerly (bottom) flow. A set of CS represents 4-hour averages constructed with data from periods when all SA operated simultaneously. Daytime behavior (11-15 LST) is summarized in Figures 7 and 8, and nighttime behavior (23-3 LST) in Figure 9. The role of WS is also explored in Figure 8, which was constructed for WS_{ref} values twice as large as those in Figure 7.

Although WS_{ref} differ with respect to Figure 5, local flow patterns are generally similar. Background roughness associated with the upwind environment, however, is now evident from $WS_{above_H} \ll WS_{ref}$. This difference is larger under northerly flow, when the arriving flow has interacted with relative high surface roughness from the Norman urban core.

4.3.1. Daytime behavior of SHFX

During daytime, the most evident feature is the increase in SHFX magnitudes with height. This is expected within the RSL from a general increase of vertical temperature and velocity gradients with height. Accordingly, the largest SHFX gradients occur

within the shear layer (near and above H), where vertical velocity gradients are maximized. Inside the canopy, vertical gradients are more homogeneous and so are SHFX fields.

SHFX distribution inside the courtyard or canyon is more homogeneous, but horizontal gradients become important. These result mostly from a combination of (1) advection by local circulations and (2) diffusion by turbulent mixing. Advection of near-ground low SHFX by the canyon rotor leads to low values near the lower lee end. These are then advected upwards by rising flow near the walls, and ultimately lead to a region of very large SHFX gradients between the upper lee end of the canyon and the lowest part of the shear layer. As the flow progresses downwind along the upper part of the canyon, SHFX magnitudes gradually increase from (1) downward mixing of turbulence from above the canyon and (2) downward advection of high SHFX values found above as well. Turbulence mixing also leads to SHFX gradient diffusion, which leads to a more homogeneous SHFX distribution in the canyon downwind side. The effects of turbulent mixing are also evident in the shear layer, where above-canyon air mixes with in-canyon air. This leads to a SHFX decrease and a SHFX gradient decrease with distance away from the upwind building edge.

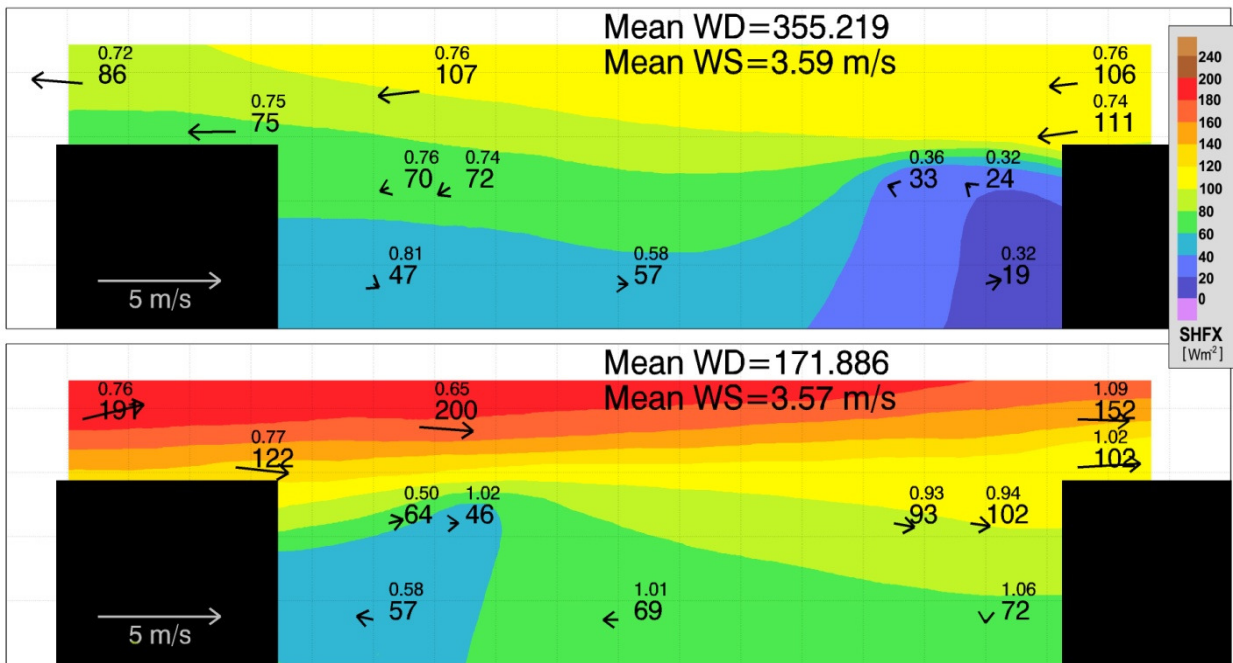


Figure 7. SHFX [Wm⁻²] (large numbers and shading), TKE [m²s⁻²] (small numbers) and wind vectors under north (top) and south (bottom) WD regimes with an average WS in the order of 3.5 ms⁻¹. Quantities represent averages over the 11-15 LST period (middle of the day), whenever data from all masts were available.

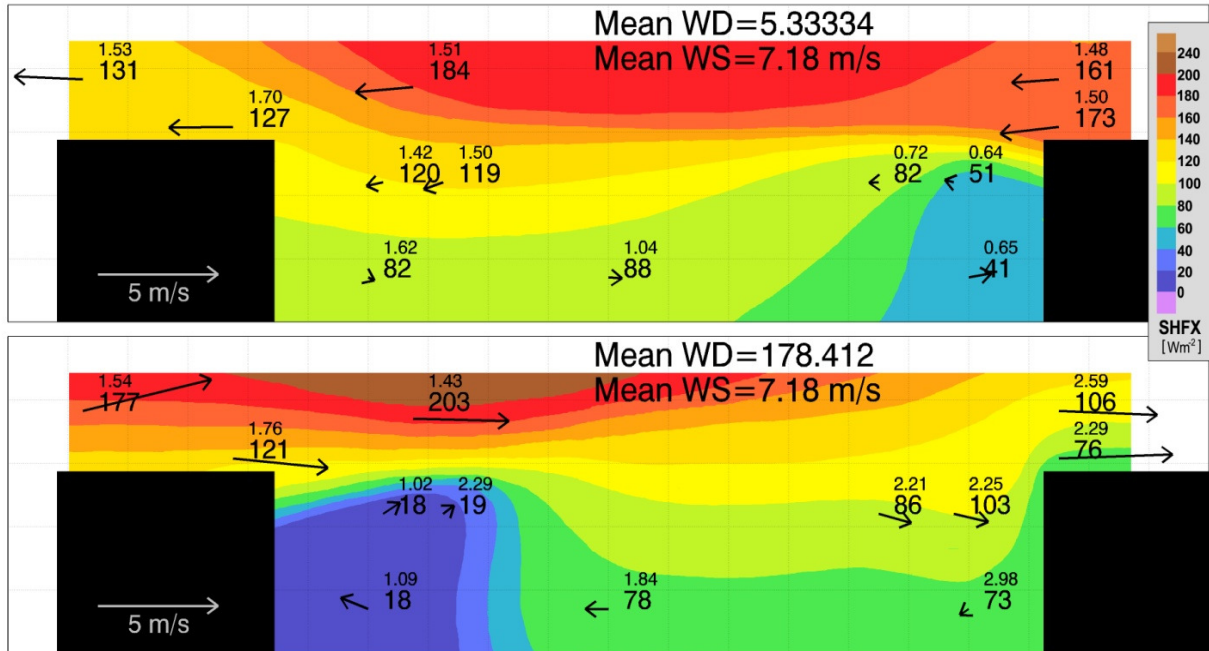


Figure 8. SHFX [Wm^{-2}] (large numbers and shading), TKE [m^2s^{-2}] (small numbers) and wind vectors under north (top) and south (bottom) WD regimes with an average WS in the order of 7.2 ms^{-1} . Quantities represent averages over the 11-15 LST period (middle of the day), whenever data from all masts were available.

4.3.2. Effects of WS

The effects of WS are explored by comparing Figures 7 and 8. As expected, both local WS and TKE values are higher in Figure 8. Larger WS lead to increases in vertical shear and turbulence intensity. Vertical shear itself leads to a general increase in SHFX. Stronger turbulence leads to increased mixing with (1) larger SHFX being mixed downwards and (2) more efficient diffusion of gradients along the direction of the flow. This explains differences found in the shear layer between Figures 7 and 8.

Increases in WS also lead to increases in the magnitude of SHFX gradients. This, however, also involves a localized decrease in SHFX values ($\sim 50 \text{ Wm}^{-2}$ in Figure 7 to below 20 Wm^{-2} in Figure 8) in the leeward corner when southerly winds are present. This decrease suggests that advection by the canyon rotor is important, and dominates when WS are large. In the case of northerly flow the local decrease in SHFX with increasing WS is not evident, but is partly masked by relatively low SHFX values being advected into the measurement site. The properties of air masses advected into the sampling domain are also a function of WS (and WD), and they can vary largely when the upwind environment is characterized by large heterogeneity. This needs to be explored with more detail.

4.3.3. SHFX during nighttime

An average distribution of SHFX during nighttime is explored in Figure 9. Following an analogy to the processes that dominate during daytime, SHFX magnitudes increase with height due to an increase in vertical temperature and velocity gradients away from the ground. The increase is not very evident for northerly winds when smaller SHFX associated with the Norman urban core are advected into the site. SHFX along the shear layer also decrease in magnitude and so do the gradients, from turbulent mixing with cooler in-canyon air.

Inside the canyon, SHFX distribution is complex and the processes that control it are not yet quite evident. A more thorough analysis is required, and the distribution will be briefly addressed in the following. Values range from from negative to neutral, and in some instances slightly positive near the downstream end. The tendency towards neutrality suggests that temperature is better mixed inside the canyon than during daytime. Stable gradients in the upwind end versus unstable ones downwind are consistent for both contrasting flow regimes. This suggests that low-level warming and/or upper-level cooling sources are present in this region. SHFX time series and the behavior of other variables need to be analyzed to investigate the causes behind this configuration.

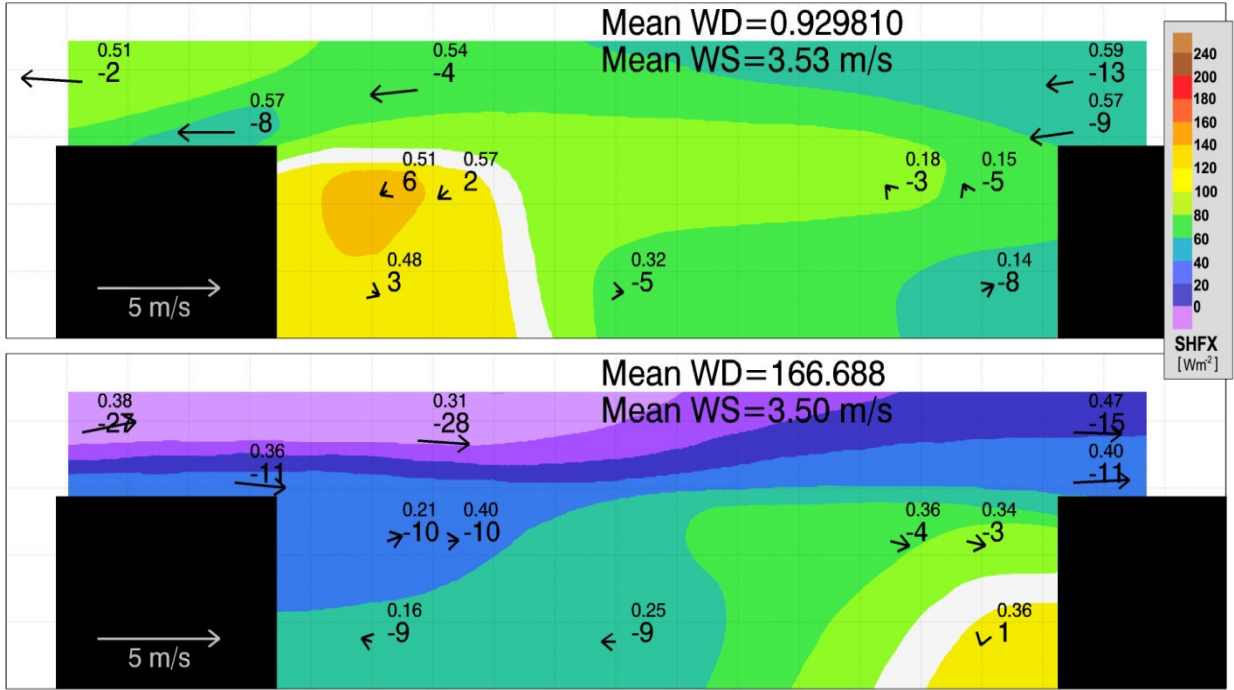


Figure 9. SHFX [Wm^{-2}] (large numbers and shading), TKE [m^2s^{-2}] (small numbers) and wind vectors under north (top) and south (bottom) WD regimes with an average WS in the order of 3.5 ms^{-1} . Quantities represent averages over the 23-3 LST period (middle of the night), whenever data from all masts were available.

5. GENERALS ON SCINTILLOMETER DATA

Scintillometer measurements were made during the length of the analysis period. Given that the data still requires some processing, only the general results and their implications are discussed.

Two prominent sources of error modulate SLS measurements and need to be addressed before moving into the analysis. The first is the set of MOS empirical functions used to determine SHFX from scintillations. These can be established via empirical fits using dissipation rate values, and can be tuned to satisfy characteristics of the urban environment, as described in section 2.2. The following expressions, not yet modified for the urban environment were used: for unstable conditions, ($\zeta < 0$):

$$C_T^2(\kappa z)^{2/3} \theta_*^{-2} = \varphi_{C_T}(\zeta) = 4\beta_1 [1 - 7\zeta + 75\zeta^2]^{1/3} \quad (1)$$

$$\epsilon \kappa z u_*^{-3} = \varphi_\epsilon(\zeta) = (1 - 3\zeta)^{-1} - \zeta \quad (2)$$

and for stable conditions ($\zeta > 0$):

$$C_T^2(\kappa z)^{2/3} \theta_*^{-2} = \varphi_{C_T}(\zeta) = 4\beta_1 [1 + 7\zeta + 20\zeta^2]^{1/3} \quad (3)$$

$$\epsilon \kappa z u_*^{-3} = \varphi_\epsilon(\zeta) = [1 + 4\zeta + 16\zeta^2]^{1/2} \quad (4)$$

where $\zeta = z/L$, z is the measurement height above ground, L is the Monin-Obukhov Length and $\beta_1 = 0.86$ is the Obukhov-Corsin constant. The second important source of error is the determination of an appropriate value for z and displacement height d_0 . The latter are particularly critical in the urban environment, and are a function of WD and WS. For the analysis, a value of $z = H = 12 \text{ m}$ was considered, and a fixed value of $d_0 = 6$ was used for simplicity. Details on the determination of appropriate d_0 values will not be discussed in this document. Accordingly, the values for z in the algorithm were replaced by $z_{\text{algor}} = z - d_0 = 6 \text{ m}$.

SLS-SA inter-comparison is summarized in Figures 10 and 11. Figure 10 shows SA and SLS timeseries during selected time periods (April 7 through April 14 2010). SLS data is shown in black and data from SA located along the SLS path in pastel colors (E1 in pink, B2 in salmon, C2 in light green and B1 in light blue). WD and WS are also shown in the lower panels in blue and red. Figure 10 reveals that, in general, SLS SHFX behave in a similar fashion than SA SHFX. The best agreement is found during unstable conditions. Diurnal cycles of SLS SHFX behave in a similar manner with respect to those of SA. SLS curves are closer to those of the SA located at 12 mAGL and SHFX values are lower to

those measured at the courtyard 15-mAGL (pink). During stable conditions, significant overestimation seems to occur frequently, and this increases as the night progresses from a decrease in WS that will be discussed later on. Problems near neutral conditions are also evident, where SLS SHFX are much higher

than SA SHFX in magnitude. Scintillometry issues near neutrality are described in the literature and were also encountered during data analysis from the suburban campaigns. They are related to reduced sensor sensitivity when scintillations are weak.

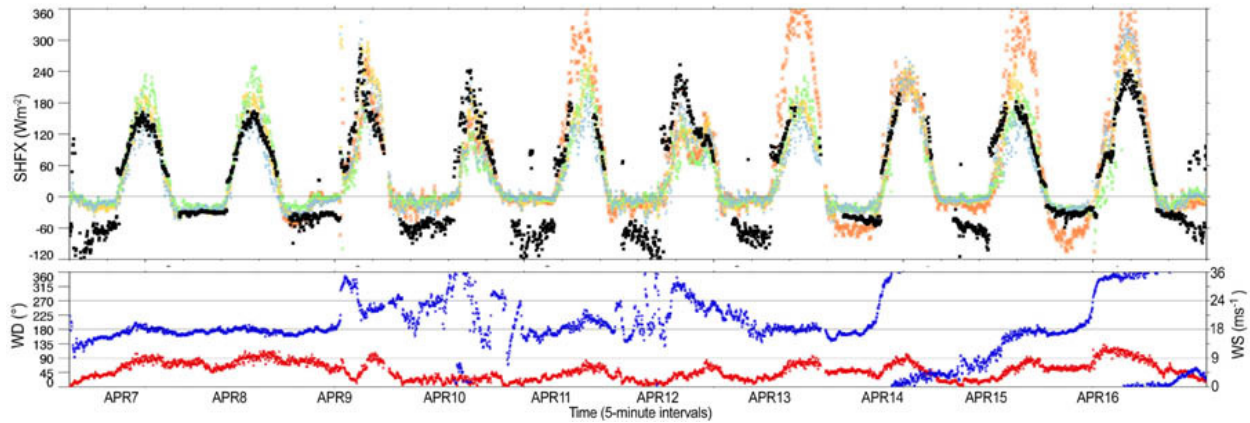


Figure 10. Selected timeseries (April 7-16) that shows comparisons between SA data (pastel colors) and SLS data (black). WD and WS are shown in blue and red.

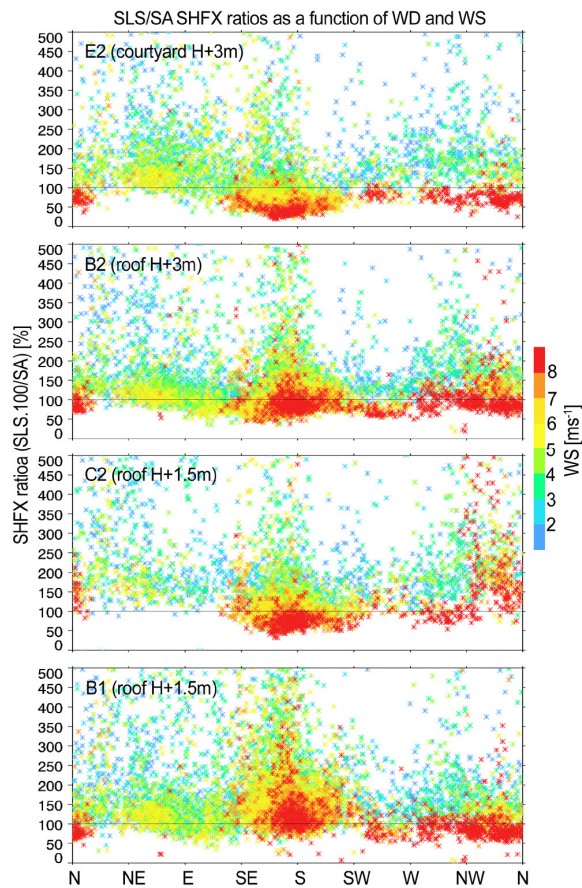


Figure 11. SLS-SA SHFX ratios (SLS*100/SA) in %, plotted as a function of WD (x-axis) and WS (color scale). Inter-comparisons are shown for four SA (four panels) located along the SLS path.

Differences can also be attributed to WD and WS. SLS SHFX tend to be larger when WS are weaker and WD from the north. Conversely, smaller values are measured under southerly flow and higher WS. Figure 11 was constructed to explore the effects of WS and WD with further detail. It consists of the SLS - SA SHFX ratios (in %) plotted as a function of WD (x-axis) and WS (color scale). The differences are calculated for the four different sonic anemometers (E2, B2, C2, B1) placed along the SLS path (similarly to Figure 10), and are presented in individual panels per SA. Figure 11 was constructed only for unstable conditions, since the performance of the SLS is the best under this type of stability regime.

Figure 11 suggests that the relation between SLS and SA SHFX is highly dependent on WS, WD and the position of the SA along the SLS path. The relationship with WS is pretty clear according to the plots. Higher WS (red) lead to smaller SLS fluxes lower WS (blues and greens) lead to higher SLS SHFX. The magnitude of over/underestimation varies among position along the path, but in general, the effects of WS are consistent. Some dependence on WD is also evident. For mast E2, SLS fluxes are lower than SA SHFX whenever along-canyon (east/west) WD prevail. When south WD occur, SHFX tend to be lower than SA SHFX for the most part. The relationships with respect to position along the path are also evident. Mast E2 shows the largest discrepancies, and this may be related to the position above the courtyard and well into the shear layer. SA

that are located closer to the roofs exhibit less discrepancies. In general, larger SLS SHFX occur in the southern part of the courtyard (E2 and C2) under southerly flow, which is consistent with higher SHFX advected into the area when winds are from the south (section 4). Also, notice that a fixed value of d_0 was used, but its dependence on WS and WD should be considered and should help to even out the differences.

Future tasks include (1) the determination of an appropriate value of d_0 , which should be a function of WD and WS; (2) the determination of appropriate adjustments to MOS coefficients; and (3) The determination of an appropriate weight function applied to SA data, that allows for comparison of scintillometer data with the observations collected using SA along the path.

6. SUMMARY AND CONCLUDING REMARKS

Within the context of ILREUM; flow and SHFX variability in the urban canopy and the lower part of the RSL were studied. This was done using SA and SLS observations collected across an environment that resembled an urban street canyon. The focus concentrated on the SHFX behavior when across-canyon reference flow was present.

The results suggest that SHFX within the canopy is regulated by (1) surface properties and their interaction with solar radiation; (2) advection by local circulations and (3) turbulent mixing; all in local and regional scales.

Canyon effects on SHFX include: (1) flow modification, (2) a decrease in vertical gradients downwind and also inside the canyon, (3) a decrease in SHFX values inside the canyon and (4) a generation of horizontal components in the gradients found inside the canyon, on top of some additional complex interactions at the local scale. Flow modification includes the development of a strong shear layer located near H ; subsiding motions across most of the shear layer and into the canyon; the development of lateral (east/west) flow exit regions; and the development of a rotor inside the canyon with a region of return flow at lower levels. Vertical gradients decrease from both advection and turbulent mixing. These mechanisms also promote the homogenization of vertical gradients inside the canyon which leads to the decrease in SHFX magnitudes. Finally, horizontal gradients arise inside the canyon from a combination between the effects of morphology on differential heating and on the flow: advection from the canyon rotor seems important.

REFERENCES

- Kanda, M., R. Moriwaki, M. Roth and T. Oke, 2002: Area-averaged sensible heat flux and a new method to determine zero-plane displacement length over an urban surface using scintillometry. *Boundary Layer Meteorology*, Volume 105, 177-193.
- Roth, M., J.A. Salmond and A.N.V. Satyanarayana, 2006: Methodological considerations regarding the measurement of turbulent fluxes in the urban roughness sublayer: the role of scintillometry. *Boundary Layer Meteorology*, Volume 121, 351-375.
- Salmond, J. A., M. Roth, T. R. Oke, A. N. V. Satyanarayana, and A. Christen, 2003: Methodological considerations regarding the use of scintillometers in the urban roughness sub-layer. EGS - AGU - EUG Joint Assembly, Abstracts from the meeting held in Nice, France, 6 - 11 April 2003.